Publ. Astron. Soc. Japan (2019) 71 (1), 5 (1–8)
doi: 10.1093/pasj/psy097
Advance Access Publication Date: 2018 September 13

On surface brightness and flux calibration for point and compact extended sources in the AKARI Far-IR All-Sky Survey (AFASS) maps

Toshiya Ueta,[1,*] Ryszard Szczerba,[2] Andrew G. Fullard,[1] and Satoshi Takita[3,†]

[1]Department of Physics and Astronomy, University of Denver, 2112 East Wesley Ave., Denver, CO 80208, USA
[2]Nicolaus Copernicus Astronomical Centre, PAS, ul. Rabiańska 8, 87-100 Toruń, Poland
[3]Institute of Space and Astronautical Science, Japan Aerospace Exploration Agency, 3-1-1 Yoshinodai, Chuo-ku, Sagamihara, Kanagawa 252-5210, Japan

*E-mail: toshiya.ueta@du.edu
†Present address: National Astronomical Observatory of Japan, 2-21-1 Osawa, Mitaka, Tokyo 181-8588, Japan.

Received 2018 May 28; Accepted 2018 July 31

Abstract

The AKARI infrared astronomical satellite produced all-sky survey (AFASS) maps in the far-infrared at roughly arcminute spatial resolution, enabling us to investigate the whole sky in the far-infrared for objects having surface brightnesses greater than a few to a couple of dozen MJy sr^{-1}. While the AFASS maps are absolutely calibrated against large-scale diffuse emission, it was uncertain whether or not an additional flux correction for point sources was necessary. Here, we verify that calibration for point-source photometry in the AFASS maps is proper. With the aperture correction method based on the empirical point spread function templates derived directly from the AFASS maps, fluxes in the AKARI bright source catalogue (BSC) are reproduced. The AKARI BSC fluxes are also satisfactorily recovered with the 1σ aperture, which is the empirical equivalent of an infinite aperture. These results confirm that in the AFASS maps far-infrared photometry can be properly performed by using the aperture correction method for point sources and by summing all pixel values within an appropriately defined aperture of the intended target (i.e., the aperture photometry method) for extended sources.

Key words: atlases — methods: data analysis — surveys — techniques: image processing — techniques: photometric

1 Introduction

The AKARI infrared astronomical satellite (Murakami et al. 2007) is the Japanese infrared space mission launched on 2006 February 21 (UT). The primary mission of AKARI was to conduct an all-sky survey in the mid- and far-infrared at higher spatial resolutions and over a wider spectral range than its predecessor, the Infrared Astronomy Satellite (IRAS: Neugebauer et al. 1984). For this purpose, AKARI was outfitted with a cryogenically cooled telescope with a diameter of 68.5 cm and two instruments, the Far-Infrared Surveyor (FIS: Kawada et al. 2007) and the Infrared Camera (IRC: Onaka et al. 2007), covering a wavelength range of 2–180 μm. AKARI carried out its 550 day cryogen mission until it exhausted its liquid helium on 2007 August 26, and

continued its post-cryogen mission in the near-infrared until the satellite was finally switched off on 2011 November 24.

The FIS instrument covers the wavelength range of 50–180 μm with two sets of Ge:Ga arrays, the short-wavelength (SW) and long-wavelength (LW) detectors in the *N60* (50–80 μm) and *WIDE-S* (60–110 μm) bands and the *WIDE-L* (110–180 μm) and *N160* (140–180 μm) bands, respectively (Doi et al. 2002; Fujiwara et al. 2003). Pixel scales in the detectors were designed to be similar to the diffraction limit of the telescope, at around 30″. For the all-sky survey, the natural 100 min sun-synchronous orbit of AKARI was used to achieve a scan speed of 36 s^{-1} during the survey period from 2006 April to 2007 August, allowing coverage of over 96% of the sky with two or more scans, and in fact resulted in 99% sky coverage (Doi et al. 2015; Takita et al. 2015).

The primary absolute surface brightness calibration of the FIS instrument was done through (1) pre-launch laboratory measurements of a blackbody source which indicated a 5% accuracy, and (2) on-orbit measurements of infrared cirrus regions without significant small-scale structures and comparisons of the results between FIS and the DIRBE instrument on-board the COBE satellite (Matsuura et al. 2011). The additional absolute calibration of the AKARI Far-infrared All-Sky Survey (AFASS) images was done, especially for very bright regions along the Galactic plane, via iterative comparison between the surface brightnesses in the AFASS images and expected surface brightnesses based on the DIRBE zodi-subtracted mission average (ZSMA) data set (Hauser 1998) augmented with the Gorjian zodiacal emission model (Gorjian et al. 2000). The resulting uncertainties were determined to be less than 10% for surface brightnesses greater than 10, 3, 25, and 26 MJy sr^{-1} at the *N60*, *WIDE-S*, *WIDE-L*,and *N160* bands, respectively, at the spatial resolution of DIRBE at approximately half a degree (Boggess et al. 1992; Takita et al. 2015).

Hence, the presently archived AFASS mapping data (Public Release Version 1, AFASSv1 hereafter, Doi et al. 2015; Takita et al. 2015)[1] should give correct surface brightnesses of diffuse background emission. However, when aperture photometry was performed for a set of infrared flux calibrators detected in the AFASS maps in the *N60*, *WIDE-S*, and *WIDE-L* bands, the resulting fluxes came out to be roughly 30%–60% less than expected (Arimatsu et al. 2014). In addition, Takita et al. (2015) compared fluxes listed in the AKARI/FIS All-Sky Bright Source Catalogue Ver. 1 (BSCv1: Yamamura et al. 2009) and those measured from the corresponding sources in the AFASS images via aperture photometry (with a 90″ radius aperture and 120″–300″ radius sky annulus) and noted that the ratio of the AFASS-to-BSC fluxes as a function of the number of sources within 5′ of the detected source (NDENS) was found to become large for NDENS $\geq$ 1 because of contamination by nearby sources. Note that the absolute flux calibration for the BSCv1 fluxes was done directly from the time-series detector signal readouts of photometry reference objects without making surface brightness maps (Yamamura et al. 2009).

As for the origin of the observed discrepancy between the observed and expected fluxes of point sources, Arimatsu et al. (2014) offered two possible explanations: (1) the observed point-source fluxes are always underestimated because of the extended point spread function (PSF) component beyond the aperture radius (e.g., Arimatsu et al. 2011), and (2) the sensitivity of the FIS detector may be lower for point sources than for diffuse sources because the signal from the point sources can be missed due to the slow transient of the FIS detector (Shirahata et al. 2009; Ueta et al. 2017). However, Doi et al. (2015) discussed in detail the slow transient effects in the AFASS data and how they were mitigated and removed. Thus, the observed flux underestimates are more likely caused by the unobserved extended PSF component beyond the 90″ aperture radius.

Thus, in the present work, we examine whether the missing extended surface brightness component is truly the cause of the observed flux underestimates for point sources. Arimatsu et al. (2014) and Takita et al. (2015) previously measured fluxes of stars in the Cohen catalogue (Cohen et al. 1999), which contains IR photometric standard stars with a flux range of 0.02–10 Jy in the *WIDE-S* band. Because of the relative faintness of these Cohen standard stars, many of them fall outside of the AKARI detection limit and their subsequent analyses were conducted using a stacking method to improve on the signal-to-noise ratio (S/N). Here, we take a different approach to verify the point-source flux calibration of the AFASS images. First, we establish the empirical PSF of the AFASS images in all four bands from the AFASS maps themselves (section 2). Then, we perform point-source photometry using the aperture correction factors derived from the empirical PSF templates as well as contour photometry with the 1 σ aperture that simulates an infinite aperture (section 3), before summarizing the entire work (section 4).

2 Establishing the empirical PSFs in the AFASS images

2.1 Source selection

First, we need to identify a set of point sources in the AFASS images as PSF/photometric references to perform

[1] In the Data ARchives and Transmission System (DARTS) maintained by the Institute of Space and Aeronautical Science (ISAS) of the Japan Aerospace Exploration Agency (JAXA): ⟨http://www.darts.isas.jaxa.jp/astro/akari/⟩.

photometry and assess the quality of flux calibration for point sources. Arimatsu et al. (2014) and Takita et al. (2015) adopted a set of 352 photometric standard stars (Cohen et al. 1999) for their analysis. However, because these Cohen stars are usually used as optical and near-IR photometry standard stars, they are not intrinsically bright in the far-IR (their expected flux is less than 10 Jy in the *WIDE-S* band). Because Arimatsu et al. (2014) and Takita et al. (2015) adopted only those that were detected at $2.5\,\sigma$ or greater in their analysis, they were able to use only 49, 97, and 9 stars in the *N60*, *WIDE-S*, and *WIDE-L* bands, respectively, and unable to find any suitable stars in the *N160* band. Also, typical far-IR photometric standards, such as asteroids and planets (Müller & Lagerros 2002), are not available in the all-sky survey scan AFASS images (i.e., removed as moving objects). Hence, we need to take a different approach to increase the number of sources that can serve as far-IR photometry standard stars in our analysis.

Our aim here is to provide good-quality point sources that are reasonably bright. Thus, rather than starting from some existing list of sources, we opt to create our own list of sources for which source detection is guaranteed in the AFASS images. To do so, we select sources from the AKARI FIS Bright Source Catalog Ver. 2 (BSCv2, I. Yamamura et al. 2016)[2] using the following two criteria: (1) FQUAL = 3 (the presence of the source is confirmed and its flux determined to be valid) in all four FIS bands, and (2) NDENS ≤ 2 (there are at most two nearby objects within $5'$ of the source). The BSCv2 release notes state that FQUAL = 3 and GRADE = 3 is the basic condition for selecting good-quality sources (I. Yamamura et al. 2016).[2] GRADE = 3 means that FQUAL = 3 in two or more bands, or FQUAL = 3 in one band and NSCANC ≥ 4 (the number of scans in which the source is detected). The first criterion that we adopt is therefore more stringent than the release notes recommend. This initial filtering identifies 658 well-detected relatively isolated sources.

Then, we cut out $20' \times 20'$ images centered at the coordinates of the 658 BSCv2 sources from the archived AFASS images[3] only when (1) an emission peak exists at the reported BSC coordinates with greater than $20\,\sigma$ and $10\,\sigma$ detection in the wide (*WIDE-S* and *WIDE-L*) and narrow (*N60* and *N160*) bands, respectively; (2) the emission peak of the BSCv2 source can be fit with a two-dimensional (2D) Gaussian (as the AFASS maps are constructed assuming a Gaussian beam profile: Doi et al. 2015); and (3) no brighter sources exist in the same $20' \times 20'$ cutout region.

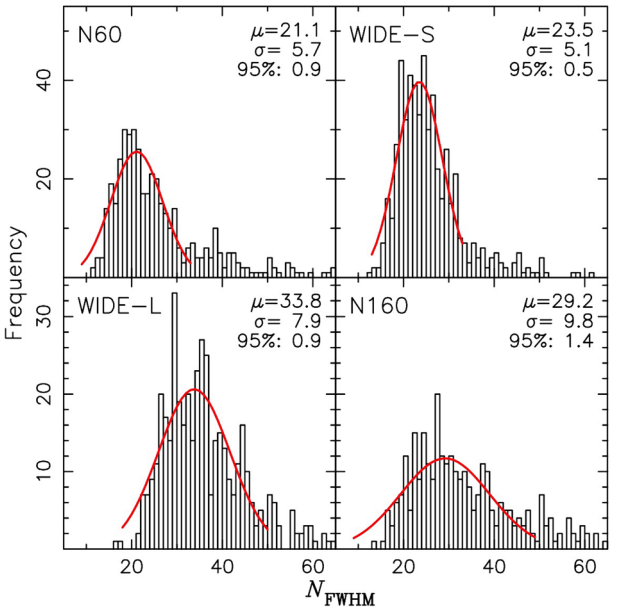

Fig. 1. Distribution of the FWHM pixel counts for the 658 BSCv2 sources in each of the four FIS bands as indicated at the top left of the frame. The Gaussian fit for each distribution is drawn by a thick line, and the mean (μ), standard deviation (σ), and 95% confidence half-interval (95%) are shown at the top right of the frame. (Color online)

Because these are BSCv2 sources, they are expected to be point sources (or point-like, at least). However, there is no guarantee that they are actually point sources. Hence, we count the number of pixels within the full-width at half-maximum (FWHM) of the peak, and determine the distribution of the FWHM pixel counts for these 658 sources in each of the four FIS bands (figure 1). The Gaussian fit to the distribution reveals the mean FWHM size (in pixel counts), standard deviation, and 95% confidence interval. We consider those that fall within the 95% confidence interval of the mean FWHM size (73, 78, 64, and 45 sources in the *N60*, *WIDE-S*, *WIDE-L*, and *N160* bands, respectively) as representative of point sources. The nature of these point sources is almost exclusively distant galaxies (about 88%), and the rest are split between stellar and unidentified objects with about equal proportions, according to their designations in the SIMBAD database[4] (cross-matched by the coordinates).

2.2 Super-PSF images

Using the AFASS cutout images of the BSCv2 point sources selected as above, we compute the normalized median

[2] Yamamura, I., Makiuti, S., & the AKARI team 2016, AKARI-FIR Bright Source Catalogue Public Version 2 Release Note. Available at ⟨http://www.ir.isas.jaxa.jp/AKARI/Archive/⟩.

[3] Each of the archived AFASS images covers a $6.^{\circ}0 \times 6.^{\circ}0$ region of sky in the ecliptic coordinates spaced by an increment of $5.^{\circ}0$.

[4] ⟨http://simbad.u-strasbg.fr/simbad/⟩.

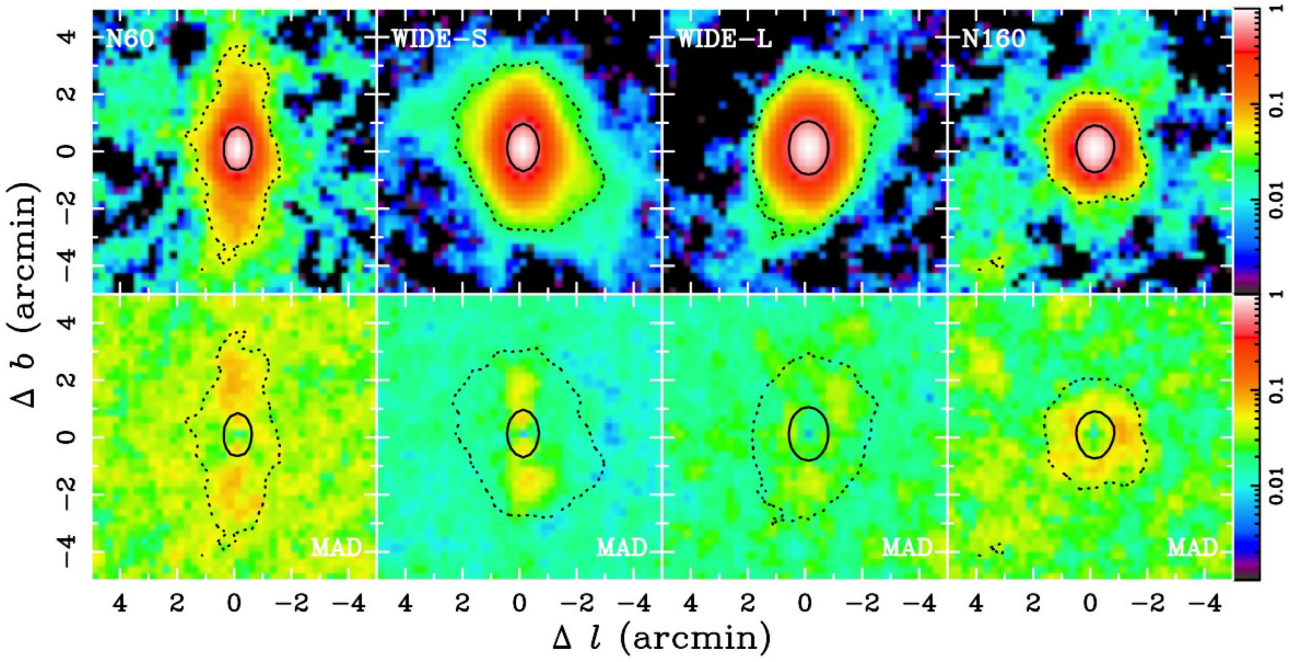

Fig. 2. AKARI/FIS super-PSF images (top row) and MAD maps (bottom row) in the *N60*, *WIDE-S*, *WIDE-L*, and *N160* bands (from left to right). The logarithmic scaling of the images, from 0.1% to 100% relative to the peak intensity, is indicated in the wedge on the right. The solid and dotted contours represent the FWHM and 5σ detection level, respectively. The image orientation follows the ecliptic coordinates, which are adopted for the original AFASS maps. (Color online)

"super-PSF" image and the corresponding median absolute deviation (MAD) map for each of the four AKARI bands (figure 2). When compiling these super-PSF images, the emission peak is fit with a 2D Gaussian function in each of the selected PSF reference images so that the PSF images are properly aligned (i.e., shifted and derotated) before being normalized and coadded. The MAD image is made by taking the median of the absolute difference between each PSF image and the super-PSF image. The MAD maps, therefore, graphically indicate how individual PSF images are statistically different (or the same) from the corresponding super-PSF image at each pixel.

Within the region that registers more than 5σ detection (the dotted contour in figure 2), the median MADs intrinsic to the source emission are determined to be 4.4 ± 1.4%, 1.5 ± 0.6%, 2.4 ± 0.6%, and 4.2 ± 1.4% for the *N60*, *WIDE-S*, *WIDE-L*, and *N160* bands, respectively. These values indicate that the shape of the adopted point sources is more than 95% identical in each of the AKARI bands, i.e., the PSF shape is fairly uniform. This uniformity among the adopted BSCv2 point sources implies that the shape of the PSF does not vary with the source brightness (i.e., the PSF is scale invariant; e.g., Ueta et al. 2017), providing the rationale to establish the super-PSF images by stacking point sources of various fluxes. In addition, comparisons with the Cohen star PSFs (Arimatsu et al. 2014) show less than 2% differences on average between the surface brightness distributions in the PSF core (i.e., within FWHM). Therefore, we adopt these super-PSF images as representative of the PSF structure in the AFASS maps.

Table 1. Super-PSF FWHM size of the AKARI/FIS all-sky survey map.

Band	In-scan FWHM (″)	Cross-scan FWHM (″)	Eccentricity
N60	96.4 ± 7.9	56.7 ± 4.1	0.81
WIDE-S	103.8 ± 5.1	68.5 ± 3.1	0.75
WIDE-L	104.2 ± 7.9	77.9 ± 7.0	0.66
N160	85.5 ± 8.3	73.3 ± 5.8	0.43

The super-PSF shape appears more elongated along the in-scan direction (i.e., along the ecliptic latitude) than along the cross-scan direction (i.e., along the ecliptic longitude) and the degree of elongation is seen more strongly in the bands at shorter wavelengths. The elongation is exhibited in both toward the ecliptic N and S directions, because sometimes the object is scanned from N to S and other times from S to N. The measured PSF/FWHM elongations and eccentricity are listed in table 1. Overall, the PSF structure in the AFASS maps based on images of the BSCv2 point sources is consistent with that based on the Cohen standard stars (table 2 of Takita et al. 2015). The FWHM sizes

of the super-PSFs are found to be larger than those found by Takita et al. (2015) for the stacked Cohen stars (1.5% to 81% with the overall averages 24.7%, 11.4%, and 37.9% for in-scan and cross-scan FWHMs, respectively). This is because the point-source FWHM size for the present analysis is determined by sheer statistics, i.e., by the most populous point-like sources (figure 1), which are not necessarily genuine point sources by nature. Also, because the present analysis deals with much brighter sources than the Cohen standards used in the previous analyses (up to an order of magnitude brighter), these stars would appear intrinsically larger.

3 Flux correction for point and compact extended sources in the AFASS maps

3.1 Photometry of the adopted point sources

In their previous analyses, Arimatsu et al. (2014) and Takita et al. (2015) used an aperture of 90″ radius and a sky annulus of 180″ width (defined between 120″ and 300″ from the target coordinates) to perform photometry with Cohen stars of their choosing. As the uncorrected-AFASS-to-BSC flux ratio, they found a constant value of 0.63 ± 0.03, 0.70 ± 0.01, and 0.38 ± 0.04 in the *N60*, *WIDE-S*, and *WIDE-L* bands, respectively. These factors were implicitly regarded as divisible photometry correction factors when photometry is done with a fixed 90″-radius aperture. For the *N160* band, the Cohen stars turned out to be too dim to allow any assessment.

Because we have now established the PSF shape in each of the four FIS bands of the AFASS, we can perform aperture photometry corrected for by the aperture correction factor based on the measured PSF shape. Using the super-PSF images and their 2D Gaussian fits, we calculate the divisible aperture correction factors as a function of the aperture size (table 2). These factors are determined based on the amount of encircled energy measured within a specific aperture defined by the relative surface brightness with respect to the peak intensity. Instead of a fixed aperture of 90″ radius, we employ the FWHM aperture (i.e., defined to be at 50% surface brightness relative to the peak) to measure the flux as the sum of pixel values within the FWHM aperture. The measured fluxes are then corrected for by the appropriate divisible correction factors (the 50% row in table 2) to recover the total flux for an infinite aperture.

The aperture-corrected fluxes of the point sources measured in our analysis are then compared against the expected fluxes listed in BSCv2. This comparison, therefore, would verify the point-source flux calibration of AFASSv1 relative to that of BSCv2. In other words, our assessment checks for internal consistency between two AKARI data products. With very limited access to far-IR photometry standard objects such as planets and asteroids in the public AFASS maps, absolute calibration is beyond the scope of the present study and we opt to seek internal consistency between AFASSv1 and BSCv2 in the present analysis.

In addition to the above aperture-corrected photometry using the FWHM aperture, we perform uncorrected photometry using the 1σ aperture (i.e., defined to be at a surface brightness equal to the sky σ) for each of the adopted point-source images at each band for comparison, because this is practically equivalent to doing photometry with the idealized infinite aperture for extended sources. Furthermore, for the sake of comparison, we perform photometry using the same 90″ aperture with the 120″–300″ sky annulus as was done by Arimatsu et al. (2014) and Takita et al. (2015).

3.2 Assessing the need for flux correction for non-diffuse sources

3.2.1 Photometry with a fixed 90″-radius aperture

First, we compare our photometry results using a fixed 90″-radius aperture against the previous results (Arimatsu et al. 2014; Takita et al. 2015). The median of the uncorrected-AFASS-to-BSCv2 flux ratios in each band is found to be 0.67 ± 0.08, 0.70 ± 0.07, 0.68 ± 0.11, and 0.69 ± 0.19 for the *N60*, *WIDE-S*, *WIDE-L*, and *N160* bands, respectively. These values indicate that roughly 70% of the expected flux is accounted for within the fixed 90″-radius aperture in all bands. We see excellent agreement in the SW bands with respect to the previous results (0.63 ± 0.03 and 0.70 ± 0.01 in the *N60* and *WIDE-S* bands, respectively), while our measurements are much better than previously reported in the *WIDE-L* band (0.38 ± 0.04). Takita et al. (2015) reported an increasing trending in the uncorrected-AFASS-to-BSCv2 flux ratio with the increasing BSCv2 flux in the *N60* band for objects less than 1 Jy, which was not seen in their preliminary analysis (Arimatsu et al. 2014) due to their use of the preliminary data. In the *WIDE-L* band, the BSCv2 sources used in our analysis are brighter (5.2–27.5 Jy) than Cohen stars adopted previously (less than 3 Jy). Thus, there may be a similar increasing trending in the *WIDE-L* band beyond 3 Jy which was not recognized previously by Takita et al. (2015).

In fact, a fixed 90″-radius aperture of the super-PSFs would translate to apertures defined by the surface brightness at 20 ± 9%, 27 ± 8%, 34 ± 8%, and 28 ± 7% of the peak intensity at *N60*, *WIDE-S*, *WIDE-L*, and *N160*, respectively. Each of these would further translate to an

Table 2. Aperture correction factors.

Aperture* (%)	*N60*	*WIDE-S*	*WIDE-L*	*N160*
90	0.071 ± 0.002	0.093 ± 0.001	0.084 ± 0.001	0.088 ± 0.001
80	0.208 ± 0.003	0.187 ± 0.003	0.176 ± 0.001	0.186 ± 0.002
70	0.258 ± 0.004	0.240 ± 0.003	0.301 ± 0.002	0.318 ± 0.003
60	0.311 ± 0.005	0.366 ± 0.004	0.406 ± 0.002	0.386 ± 0.004
50	0.426 ± 0.006	0.419 ± 0.005	0.463 ± 0.003	0.493 ± 0.005
40	0.497 ± 0.007	0.510 ± 0.005	0.559 ± 0.003	0.576 ± 0.007
30	0.546 ± 0.008	0.597 ± 0.006	0.646 ± 0.004	0.668 ± 0.008
20	0.652 ± 0.009	0.682 ± 0.007	0.751 ± 0.005	0.769 ± 0.010
10	0.737 ± 0.012	0.757 ± 0.008	0.853 ± 0.006	0.871 ± 0.012
8	0.766 ± 0.013	0.792 ± 0.008	0.861 ± 0.006	0.893 ± 0.013
5	0.800 ± 0.013	0.830 ± 0.008	0.911 ± 0.006	0.921 ± 0.014
1	0.895 ± 0.017	0.913 ± 0.009	0.978 ± 0.008	0.986 ± 0.015

*The aperture size is defined by the percentage of the peak intensity.

aperture correction factor of 0.7 to 0.57, i.e., the 90″-radius apertures would typically cover 60% to 65% of the total flux across the bands (table 2). This is consistent with the median uncorrected-AFASS-to-BSCv2 flux ratio being about 68% across the bands. Hence, we consider that our results are robust and confirm that the previously reported flux underestimates at around 40% were caused by the use of the fiducial 90″ aperture that did not account for the surface brightness component beyond the aperture.

3.2.2 Photometry with the derived aperture correction

Second, we compare our photometry results using the FWHM (50% peak) aperture corrected for by the corresponding correction factor. With the aperture correction method, the corrected-AFASS-to-BSCv2 flux ratio is found to be 0.97 ± 0.14, 0.94 ± 0.10, 0.92 ± 0.10, and 0.82 ± 0.22. The derived ratio as a function of the BSCv2 flux for each band is shown in figure 3.

Here, we confirm that the BSCv2 fluxes for the adopted point sources are reproduced within the margin of error by means of the aperture correction method. As we saw in the previous section, the use of a 90″-radius aperture would generally result in about 40% flux underestimates, while this 90″-radius aperture would require flux correction by a divisible factor of about 0.6 (table 2). Raw fluxes are underestimated because of an extended PSF component beyond the aperture radius, as previously considered by Arimatsu et al. (2011). The present results verify the expectation that BSCv2 point-source fluxes can be recovered from the AFASS maps by aperture photometry with proper aperture correction.

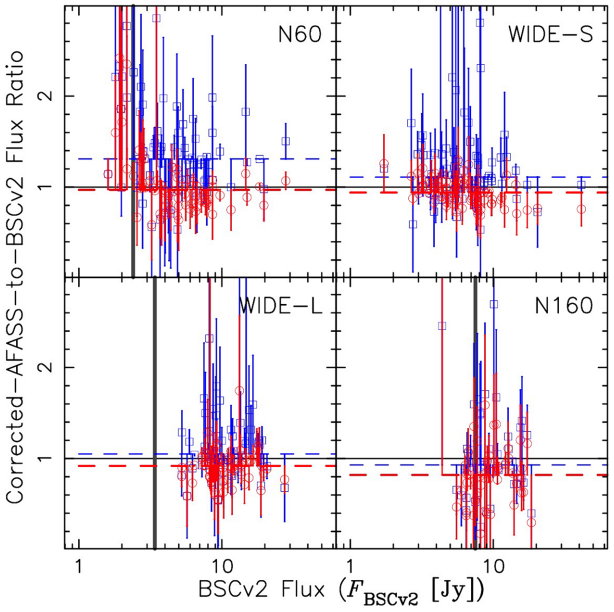

Fig. 3. Corrected-AFASS-to-BSCv2 flux ratio vs. the BSCv2 flux for each of the four AKARI/FIS bands as indicated at the top right corner. Circles show the ratios based on the aperture correction method, while squares are those based on the $1\,\sigma$ aperture method. Corresponding error bars in the ratio are also shown. The black solid horizontal line shows the unity ratio, whereas the red and blue dashed lines indicate the median ratio for the aperture correction and $1\,\sigma$ aperture methods, respectively. The relatively large scatters in the flux ratio are also previously reported by Takita et al. (2015) and were attributed to the difference in the actual photometry methods with the AFASS maps and in the BSC. The vertical thick gray lines indicate the BSCv2 detection limit (I. Yamamura et al. 2016) 2 at 2.4, 0.44, 3.4, and 7.5 Jy in the *N60*, *WIDE-S*, *WIDE-L*, and *N160* bands, respectively (where visible). (Color online)

3.2.3 Photometry with the $1\,\sigma$ aperture without correction

Third, we compare our photometry results using the $1\,\sigma$ aperture without any aperture correction. This method practically corresponds to photometry using an infinite

aperture. We employ this method of photometry in particular because photometry results must be verified not only for point sources but also for extended sources. With this method, the AFASS-to-BSCv2 flux ratio is derived to be 1.31 ± 0.29, 1.11 ± 0.20, 1.05 ± 0.19, and 0.93 ± 0.21. The derived ratio as a function of the BSCv2 flux for each band is also shown in figure 3.

These measurements indicate that the BSCv2 fluxes are reproduced reasonably well by setting the photometry aperture at the "edge" of the point sources (defined by the $1\,\sigma$ contour), while uncertainties become correspondingly higher (as the number of lower-S/N pixels in the photometry aperture is larger). However, the measured fluxes in the *N60* band appear to be overestimated by $31 \pm 29\%$. This flux overestimate in the *N60* band can be attributed to the inevitable elongation of the bright PSF core. Because a target can be scanned in both N to S and S to N directions along the Ecliptic during multiple sky coverage, the resulting AFASS map shows elongation of the PSF core in both N and S directions. This effect is seen most prominently in the *N60*-band PSF image (figure 2). Hence, the surface brightness is double-counted in the elongated parts of the PSF when photometry is done by an aperture that encompasses the entire elongation. Based on the super-PSF map in the *N60* band (figure 2), the excessively elongated parts of the PSF (e.g., $>2'$ away from the peak) register surface brightnesses at most a few tens of percent of the peak intensity. This means that at most a few tens of percent of the total flux can be accounted for in these elongated parts of the PSF (table 2), corroborating the measured $\sim$30% flux overestimate in the *N60* band. In genuinely extended sources, the distribution of surface brightness is supposedly not as centrally concentrated as in point sources. Hence, the flux overestimates seen above as a result of the source elongation would be expected to be less severe in genuinely extended sources. Therefore, we consider that both of these photometry methods work reasonably well.

3.2.4 Summary: Flux calibration in the AFASS maps

As demonstrated above, we have verified that roughly 40% flux deficiencies previously reported for point sources in the AFASS maps are caused by the adopted $90''$-radius aperture, which typically misses about 40% of the total flux distributed beyond the aperture. We also confirm that the total flux of extended sources can be recovered without any special correction by the use of an appropriate aperture that encompasses the entire extent of the extended source.

These findings suggest that the surface brightness of the AFASS maps is calibrated correctly for non-diffuse sources as well as diffuse sources. Therefore, with the AFASSv1 images, we hereby confirm that (1) photometry for point sources can be done with the aperture correction method using the correction factors presented here (table 2), and (2) photometry for extended sources can be done by summing surface brightnesses within an appropriate aperture of the target source and converting the pixel value sum into flux by multiplying by 5.29×10^{-3} ([Jy] [MJy sr^{-1}]$^{-1}$) $= 2.35 \times 10^{-5}$ ([Jy arcsec^{-2}] [MJy sr^{-1}]$^{-1}$) $\times$ 15 $\times$ 15 (arcsec^2; at the default pixel scale of AFASSv1).

4 Conclusions

We present an independent photometric analysis of point sources detected in the AKARI far-IR all-sky survey maps (AFASSv1: Doi et al. 2015). By comparing with their corresponding flux entries in the the AKARI bright-source catalogue ver. 2 (BSCv2: I. Yamamura et al. 2016), 2 we establish that the surface brightness of the AFASSv1 maps has been calibrated properly for point sources and extended sources alike, in addition to large-scale diffuse emission against which the AFASS maps were originally absolutely calibrated.

In particular, we find that the suspected flux underestimates for point sources in the AFASS maps reported earlier by Arimatsu et al. (2014) and Takita et al. (2015) can be mitigated by applying a proper aperture correction. In doing so, we construct the empirical super-PSF templates ourselves (figure 2) and derive our own point-source aperture correction factors (table 2).

The BSCv2 point-source fluxes are reproduced reasonably well even when direct photometry is done with a $1\,\sigma$ photometry aperture (i.e., all the surface brightness pixel values within the aperture are summed to compute the source flux). This means that direct photometry for any source (point, extended, and diffuse) detected in the AFASS maps yields a correct flux measurement when a sufficiently large aperture is used.

On the whole, the AFASS maps are useful tools to directly measure far-IR fluxes. This is true especially for sources that are not exactly point sources (i.e., extended), because the BSC catalogue flux entries may not be appropriate for such extended sources.

Acknowledgment

This research is based on observations with AKARI, a JAXA project with the participation of ESA. TU acknowledges support and encouragement by the AKARI team at the Institute of Space and Aeronautical Science of JAXA, especially from Dr. Issei Yamamura.

References

Arimatsu, K., et al. 2011, PASP, 123, 981

Arimatsu, K., Doi, Y., Wada, T., Takita, S., Kawada, M., Matsuura, S., Ootsubo, T., & Kataza, H. 2014, PASJ, 66, 47

Boggess, N. W., et al. 1992, ApJ, 397, 420
Cohen, M., Walker, R. G., Carter, B., Hammersley, P., Kidger, M., & Noguchi, K. 1999, AJ, 117, 1864
Doi, Y., et al. 2002, Adv. Space Res., 30, 2099
Doi, Y., et al. 2015, PASJ, 67, 50
Fujiwara, M., Hirao, T., Kawada, M., Shibai, H., Matsuura, S., Kaneda, H., Patrashin, M., & Nakagawa, T. 2003, Applied Optics, 42, 2166
Gorjian, V., Wright, E. L., & Chary, R. R. 2000, ApJ, 536, 550
Hauser, M. G., et al. 1998, ApJ, 508, 25
Kawada, M., et al. 2007, PASJ, 59, S389
Matsuura, S., et al. 2011, ApJ, 737, 2
Müller, T. G., & Lagerros, J. S. V. 2002, A&A, 381, 324
Murakami, H., et al. 2007, PASJ, 59, S369
Neugebauer, G., et al. 1984, ApJ, 278, L1
Onaka, T., et al. 2007, PASJ, 59, S401
Shirahata, M., et al. 2009, PASJ, 61, 737
Takita, S., et al. 2015, PASJ, 67, 51
Ueta, T., Tomasino, R. L., Takita, S., Izumiura, H., Shirahata, M., Fullard, A., Yamamura, I., & Matsuura, S. 2017, PASJ, 69, 11
Yamamura, I., et al. 2009, in ASP Conf. Ser. 418, AKARI, a Light to Illuminate the Misty Universe, ed. T. Onaka et al. (San Francisco: ASP), 3